Article

Quantum control of a cat qubit with bit-flip times exceeding ten seconds

U. Réglade[1,2,4], A. Bocquet[1,2,4], R. Gautier[2], J. Cohen[1], A. Marquet[1,3], E. Albertinale[1], N. Pankratova[1], M. Hallén[1], F. Rautschke[1], L.-A. Sellem[2], P. Rouchon[2], A. Sarlette[2], M. Mirrahimi[2], P. Campagne-Ibarcq[2], R. Lescanne[1], S. Jezouin[1,5] & Z. Leghtas[2,5 ✉]

Quantum bits (qubits) are prone to several types of error as the result of uncontrolled interactions with their environment. Common strategies to correct these errors are based on architectures of qubits involving daunting hardware overheads[1]. One possible solution is to build qubits that are inherently protected against certain types of error, so the overhead required to correct the remaining errors is greatly reduced[2–7]. However, this strategy relies on one condition: any quantum manipulations of the qubit must not break the protection that has been so carefully engineered[5,8]. A type of qubit known as a cat qubit is encoded in the manifold of metastable states of a quantum dynamical system, and thereby acquires continuous and autonomous protection against bit-flips. Here, in a superconducting-circuit experiment, we implemented a cat qubit with bit-flip times exceeding 10 s. This is an improvement of four orders of magnitude over previously published cat-qubit implementations. We prepared and imaged quantum superposition states, and measured phase-flip times greater than 490 ns. Most importantly, we controlled the phase of these quantum superpositions without breaking the bit-flip protection. This experiment demonstrates the compatibility of quantum control and inherent bit-flip protection at an unprecedented level, showing the viability of these dynamical qubits for future quantum technologies.

Dynamical systems result from the interplay of external forces, nonlinearities and dissipation[9]. Of particular interest are bistable dynamical systems that switch between two attractors, such as the reversal of Earth's magnetic field. At a vastly reduced scale, driven nonlinear oscillators containing only a few photons have displayed switching times of several seconds[10], making them ideal candidates for ultralow-power classical logic processing[11].

It is therefore tempting to use this stability to robustly encode quantum information where susceptibility to noise is the limiting factor for the emergence of quantum machines[1]. Qubits fail in two ways: first, by random switching between computational states, known as bit-flips; and second, by the scrambling of the phase of quantum superpositions, known as phase-flips[12]. A qubit encoded in the manifold of the metastable states of a dynamical system, known as a cat qubit, would be protected against bit-flips at the hardware level. The challenge is then to measure and control this qubit without breaking that protection. If this challenge is met, the only remaining error, phase-flips, can then be corrected by embedding these qubits in error-correcting architectures, with a substantially reduced hardware overhead[2,4,6,8,13] compared with those required to correct both bit-flips and phase-flips[1,14].

Making the leap from classical to quantum information processing with dynamical bistable systems is difficult. Indeed, such systems owe their stability to friction (dissipation) that dampens the erroneous diffusion between states. However, friction commonly originates from interactions with an ensemble of degrees of freedom. This leaks information about the system, and quantum superpositions decohere into classical mixtures[15]. Surprisingly, there is a type of dissipation, known as two-photon dissipation[16–18], that provides stability without inducing decoherence. Indeed, two-photon exchanges between an oscillator and a cold environment are expected to stabilize two coherent states with macroscopic bit-flip times but allow the preparation and manipulation of their quantum superpositions[18].

In practice, two-photon dissipation is implemented in a superconducting oscillator mode, known as the memory, that is coupled to a lossy buffer mode through a nonlinear Josephson element. In previous experiments, quantum tomography of the memory was done by using an ancillary system composed of a transmon and its readout resonator. Although quantum superpositions of two metastable states were observed, the bit-flip time saturated in the millisecond range[19]. Cat-qubit implementations based on the Kerr effect reached similar timescales[20,21]. In a recent experiment[22], this tomography apparatus was removed entirely and bit-flip times exceeding 100 s were observed. However, because the two-photon exchange rate was dominated by single-photon loss, quantum superposition states could not be prepared or measured, thereby falling short of implementing a qubit. This finding motivated the removal of the ancillary transmon and the

[1]Alice & Bob, Paris, France. [2]Laboratoire de Physique de l'Ecole Normale Supérieure, ENS-PSL, CNRS, Sorbonne Université, Université Paris Cité, Centre Automatique et Systèmes, Mines Paris, Université PSL, Inria, Paris, France. [3]Ecole Normale Supérieure de Lyon, CNRS, Laboratoire de Physique, Lyon, France. [4]These authors contributed equally: U. Réglade, A. Bocquet. [5]These authors jointly supervised this work: S. Jezouin, Z. Leghtas. ✉e-mail: zaki.leghtas@ens.fr

development of an alternative tomography procedure that does not break the bit-flip protection.

In this experiment, we implemented a cat qubit with bit-flip times exceeding 10 s, which to the best of our knowledge is an improvement of four orders of magnitude over previous cat-qubit implementations, and of six orders of magnitude over the lifetime of the photons composing the qubit. We observed phase-flip times greater than 490 ns, mainly limited by single-photon loss. We controlled the phase of coherent superpositions by rotating them in a Zeno-blocked manifold[23], performing a π rotation in 235 ns. We verified that this manipulation only marginally reduced the bit-flip time, maintaining it above 10 s. This was made possible by implementing a quantum tomography protocol that required no additional ancillary elements[24]. Indeed, the Josephson dipole that mediates two-photon dissipation was used to map quantum observables of the memory onto the buffer. This experiment demonstrates the tomography and control of a cat qubit without breaking the bit-flip protection at the level of bit-flip times of 10 s. However, further improvements in state preparation, measurement fidelity and single-photon loss will be necessary before scaling up to a fully protected hardware-efficient logical qubit[5,6,8,13].

Our dynamical system is well described by the following Hamiltonian and loss operator:

$$\mathbf{H}_{2ph} = g_2^* \mathbf{a}^2 \mathbf{b}^\dagger + g_2 \mathbf{a}^{\dagger 2} \mathbf{b} - \varepsilon_d^* \mathbf{b} - \varepsilon_d \mathbf{b}^\dagger,$$
$$\mathbf{L}_b = \sqrt{\kappa_b}\,\mathbf{b}, \tag{1}$$

where $\mathbf{a}$, $\mathbf{a}^\dagger$ and $\mathbf{b}$, $\mathbf{b}^\dagger$ are respectively the memory and buffer annihilation and creation operators, ε_d is the amplitude of a resonant drive applied to the buffer, and κ_b is the buffer energy damping rate. The symbol $*$ denotes the complex conjugate. Photon pairs are dissipated from the memory by converting them at rate g_2 to single photons in the buffer, and these are then dissipated into the environment. In the absence of energy damping in the memory, the steady states of this system lie in a two-dimensional manifold[17] spanned by:

$$|\pm\rangle_\alpha = (|\alpha\rangle \pm |-\alpha\rangle)/\sqrt{\mathcal{N}_\pm}, \tag{2}$$

where the normalization factor $\mathcal{N}_\pm = 2 \pm 2\exp(-2|\alpha|^2)$ and $|\alpha\rangle$ is a coherent state of amplitude α that is controlled by the drive amplitude, $\alpha^2 = \varepsilon_d/g_2^*$. The local convergence rate towards this manifold is denoted κ_{conf} and in our parameter regime it saturates at $\kappa_{conf} \approx \kappa_b/2$ (Supplementary Information section 8C). The qubit encoded in this manifold owes its name, the cat qubit[18], to the fact that $|\pm\rangle_\alpha$ resembles the Schrödinger cat states for $|\alpha| \gtrsim 1$ (ref. 25). Its computational states are defined as $|0/1\rangle_\alpha = (|+\rangle_\alpha \pm |-\rangle_\alpha)/\sqrt{2} \approx |\pm\alpha\rangle$ and its X and Z Pauli operators as $\mathbf{Z}_\alpha \approx |\alpha\rangle\langle\alpha| - |-\alpha\rangle\langle-\alpha|$ and $\mathbf{X}_\alpha \approx |\alpha\rangle\langle-\alpha| + |-\alpha\rangle\langle\alpha|$ up to errors that are exponentially small in $|\alpha|^2$.

States $|\pm\alpha\rangle$ are localized on opposite sides of the phase space (Fig. 1a), with exponentially small support overlap in $|\alpha|^2$. Therefore, even in the inevitable presence of losses, provided they are diffusive-like[26] and weak compared with κ_{conf}, the bit-flip time T_X between $|\pm\alpha\rangle$ is expected to increase exponentially with $|\alpha|^2$ (ref. 19). From $|\alpha|^2 \approx 10$ onwards, timescales T_X exceeding seconds are predicted in our parameter regime. Quantum superpositions of $|\pm\alpha\rangle$ are prepared by initializing the memory in the vacuum and activating the two-photon exchange mechanism[17]. Because the dynamics of equation (1) conserve memory photon-number parity, the state spontaneously dissipates towards $|+\rangle_\alpha$ on a timescale set by κ_{conf}^{-1}. The state then evolves into a classical statistical mixture of $|\pm\alpha\rangle$ at rate $\Gamma_Z^{\kappa_a} = 2\kappa_a|\alpha|^2$ (ref. 25), where κ_a is the memory energy damping rate. Therefore the observation of quantum superpositions of metastable states with macroscopic bit-flip times requires that the decoherence rate verifies $\Gamma_Z^{\kappa_a} < \kappa_{conf}$ for $|\alpha^2| \approx 10$.

We implemented the dynamics of equation (1) in a two-dimensional-circuit quantum electrodynamics architecture[27] (Fig. 1b) operated in
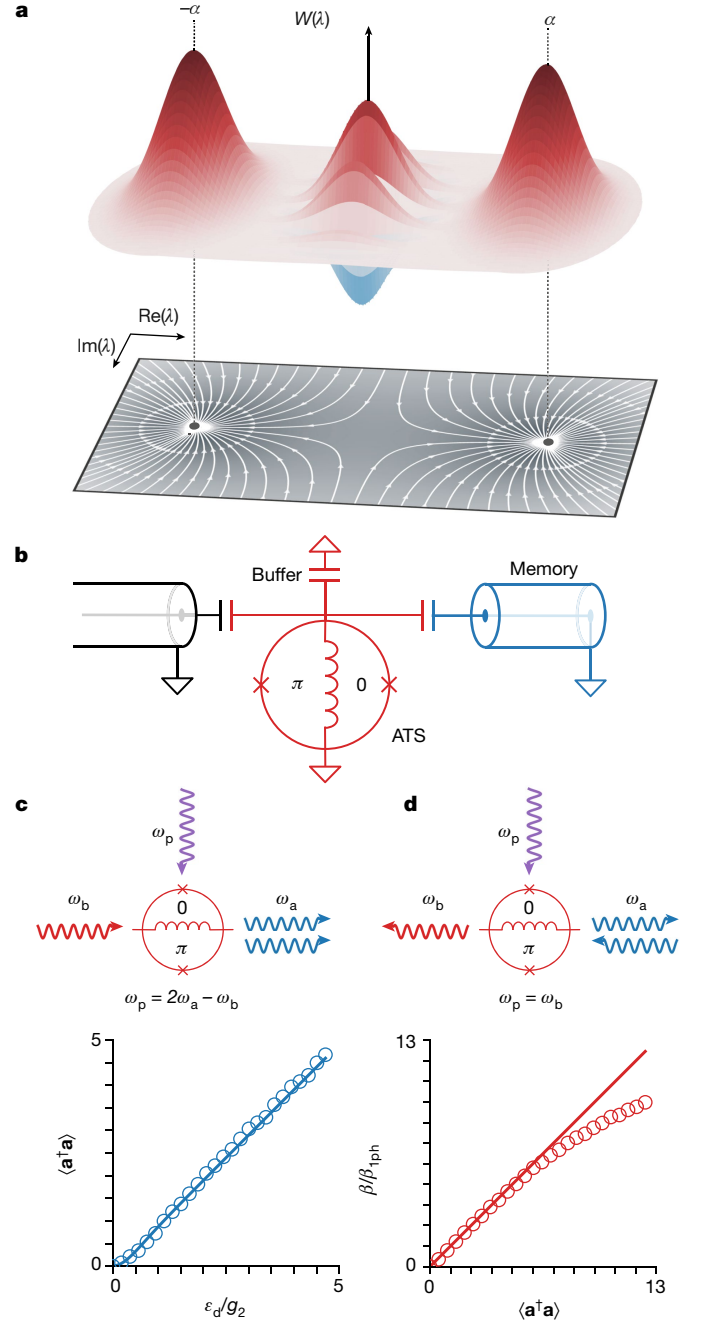
Fig. 1 | Encoding quantum information in a bistable dynamical system. **a**, Semiclassical trajectories (solid lines, derived from equation (1)) over the complex phase space (Re and Im denote the real and imaginary axes). Each trajectory converges towards one of the two metastable states. Quantum information encoded in the manifold spanned by these states (the Wigner function corresponds to a coherent superposition state) inherit protection against bit-flips. **b**, Circuit implementation of our dynamical system. A quarter-wavelength transmission line mode (memory; blue) is coupled to its environment (black) through a buffer mode (red) composed of an ATS. **c**, A pump (purple) and a buffer drive (red) combine through the ATS to inject photon pairs into the memory (blue). The reverse process, which removes photon pairs, is not shown. We measured (open circles) a linear increase (simulation in solid line) in the steady-state memory photon number (y axis) with increasing drive amplitude (x axis). **d**, A pump at frequency ω_p (purple) displaces the buffer (red) conditionally according to the number of photons in the memory (blue). This is an important part our quantum tomography protocol. We measured (open circles) the buffer amplitude (y axis) against the memory photon number (x axis) reached after a displacement pulse. The deviation from the linear trend (solid line) is a hallmark of compression resulting from higher-order processes.
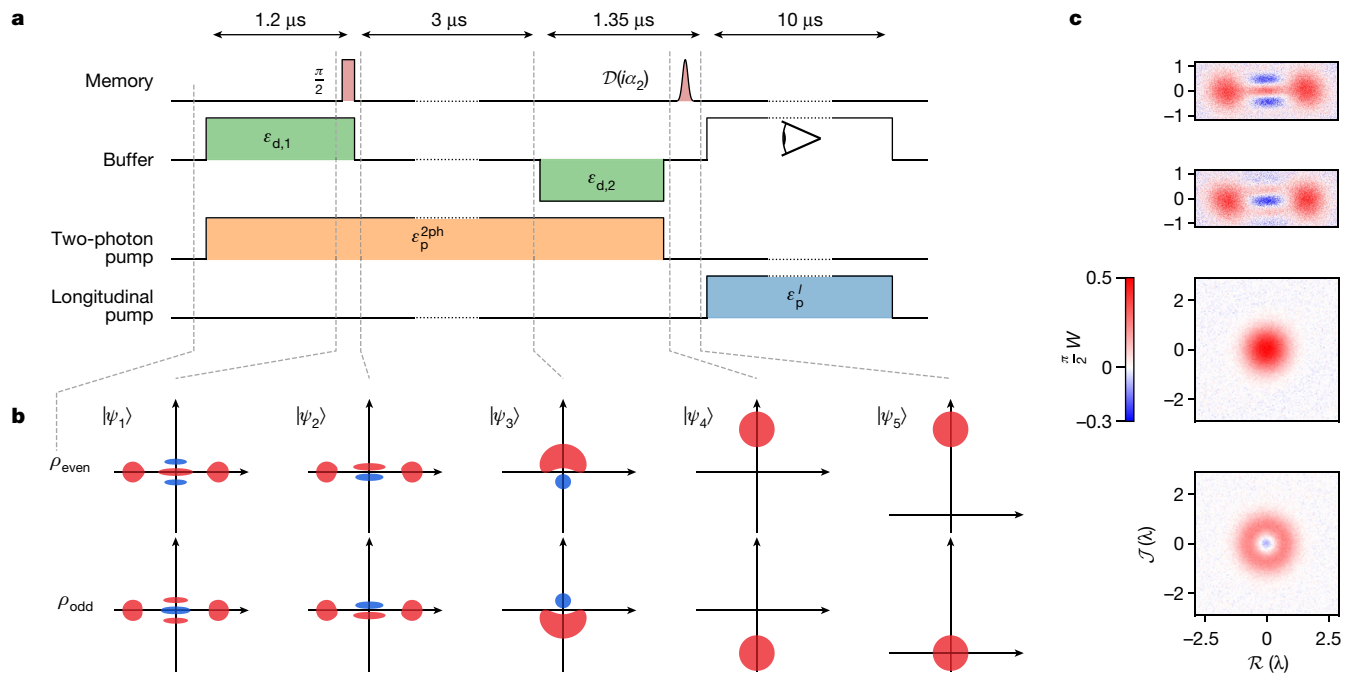
Fig. 2 | Quantum tomography protocol based on the holonomic gate[24]. a, Pulse sequence for each control channel as a function of time. The parity of the memory is mapped onto the photon number, which is measured through longitudinal coupling to the buffer. **b**, The memory Wigner function at each step (grey dashed lines) of the protocol for an even (top) and odd (bottom) initial state. **c**, Measured Wigner functions of the memory initialized in $|+\rangle_\alpha, |-\rangle_\alpha, |0\rangle$ and Fock state $|1\rangle$ (top to bottom), obtained by combining the photon parity measurement with simple memory displacements and an active memory reset (Supplementary Information section 4D). The first two images contain 250×100 pixels averaged 5,000 times, and the last two contain 100×100 pixels averaged 70,000 times. The acquisition time was 2 h and 12 h, respectively.

a dilution refrigerator at 10 mK. The chip consisted of a sapphire substrate on which we sputtered a tantalum film[28], which was then patterned. The memory is a quarter-wavelength coplanar waveguide resonator of frequency $\omega_a/2\pi = 5.26$ GHz and decay rate $\kappa_a/2\pi = 9.3$ kHz, corresponding to a lifetime of 17 μs. It is capacitively coupled to the buffer, which is composed of an island shunted to ground through a nonlinear element called the asymmetrically threaded superconducting quantum interference device (SQUID)[19], resonating at $\omega_b/2\pi = 7.70$ GHz with decay rate $\kappa_b/2\pi = 2.6$ MHz. The asymmetrically threaded SQUID (ATS) is composed of a SQUID shunted in the middle by a kinetic inductance so it forms two loops. By setting the flux to 0 and π in the right and left loops, respectively (Fig. 1b), this element induces the following nonlinear potential: $U(\varphi) \approx -2E_J\varepsilon_p(t)\sin(\varphi)$ (ref. 19), where E_J is the Josephson energy of the SQUID junctions. Here, $\varepsilon_p(t) = \varepsilon_p\cos(\omega_p t)$ is a flux pump of amplitude ε_p and angular frequency ω_p, and φ is the phase drop across the ATS, which is a linear combination of $\mathbf{a}, \mathbf{a}^\dagger, \mathbf{b}$ and $\mathbf{b}^\dagger$. Setting the pump frequency $\omega_p = 2\omega_a - \omega_b$ activates the desired third-order process $\mathbf{a}^2\mathbf{b}^\dagger + \mathbf{a}^{\dagger 2}\mathbf{b}$ (Fig. 1c) at a rate g_2 that grows linearly with the pump amplitude. The latter is increased until g_2 is about equal to κ_b, thereby maximizing κ_{conf}. We reach $g_2/2\pi = 0.76$ MHz and $\kappa_{conf}/2\pi \approx 1.3$ MHz. For $|\alpha|^2 \in [1.4, 11.3]$, this places it in the favourable regime in which $\Gamma_Z^{\kappa_a}/\kappa_{conf} \in [0.02, 0.16]$.

Josephson circuits have been referred to as the 'Swiss army knife' of microwave quantum optics[29]. Simply by switching the pump frequency, the behaviour of a dipole can be greatly altered. By setting the pump frequency to $\omega_p = \omega_b$ (Fig. 1d), the following low-order processes were resonantly selected: $(\mathbf{b} + \mathbf{b}^\dagger), \mathbf{a}^\dagger\mathbf{a}(\mathbf{b} + \mathbf{b}^\dagger)$ and $\mathbf{b}^{\dagger 2}\mathbf{b} + \mathbf{b}^\dagger\mathbf{b}^2$. The first term, $(\mathbf{b} + \mathbf{b}^\dagger)$, is cancelled out by adding an additional drive of equal amplitude and opposite phase on the buffer. The second term, $\mathbf{a}^\dagger\mathbf{a}(\mathbf{b} + \mathbf{b}^\dagger)$, is analogous to the radiation pressure coupling in optomechanics[30], and has been referred to as a longitudinal coupling in the context of Josephson circuits[31]. Conditioned on the number of photons n_a in the memory, the buffer converges towards a coherent state of amplitude

denoted as $\beta_{1ph} \times n_a$. When cascaded with a heterodyne detection of the buffer, it constitutes a quantum non-demolition measurement of the memory photon number. The third term, $\mathbf{b}^{\dagger 2}\mathbf{b} + \mathbf{b}^\dagger\mathbf{b}^2$, is a parasitic interaction that is responsible for the compression visible in Fig. 1d, and thereby limits the dynamical range of our detector. The longitudinal pump amplitude was chosen to maximize the detection efficiency over a dynamical range of 0 to about 10 photons in the memory. We reached a single-shot fidelity of 89% to distinguish between the vacuum and a coherent state containing 10 photons with an integration time of 10 μs constrained by the memory lifetime (Supplementary Information section 4B).

We witnessed the quantum nature of the memory field through Wigner tomography[25]. The Wigner quasi probability distribution W is a real function of a complex amplitude λ defined as $W(\lambda) = (2/\pi)\langle\mathbf{D}_\lambda\mathbf{P}\mathbf{D}_{-\lambda}\rangle$. It represents the normalized expectation value of the parity operator $\mathbf{P} = \exp(i\pi\mathbf{a}^\dagger\mathbf{a})$ for the state displaced by $\mathbf{D}_\lambda = \exp(\lambda\mathbf{a}^\dagger - \lambda^*\mathbf{a})$. This graphical representation can display negativities that unambiguously testify to the non-classical nature of the field state.

Our Wigner tomography protocol (Fig. 2) is based on the so-called holonomic gate proposed in ref. 24. All odd parity states are mapped onto the vacuum $|0\rangle$, and all even parity states are mapped onto a coherent state $|\psi_5\rangle = |2i\alpha_2\rangle$ in which $2\alpha_2 \approx 4.8$. The quantum non-demolition photon-number measurement through longitudinal coupling then distinguishes between $|0\rangle$ and $|2i\alpha_2\rangle$, providing a photon-number parity measurement. Our pulse sequence (Fig. 2a) alternates between memory drives, two-photon dissipation, buffer drives of various amplitudes and longitudinal coupling. We will now describe it step by step (Fig. 2b). Let us assume that the memory is initially in an even parity state, ρ_{even}. First, we activated a two-photon pump ε_p^{2ph} and buffer drive $\varepsilon_{d,1} = g_2^*\alpha_1^2$, where α_1 is real. By parity conservation, ρ_{even} is mapped to the even state $|\psi_1\rangle = |+\rangle_{\alpha_1}$. Next, we added a memory drive along the imaginary axis. Two-photon dissipation confines the dynamics to the quantum manifold spanned by $|\pm\rangle_{\alpha_1}$. The added memory drive induces
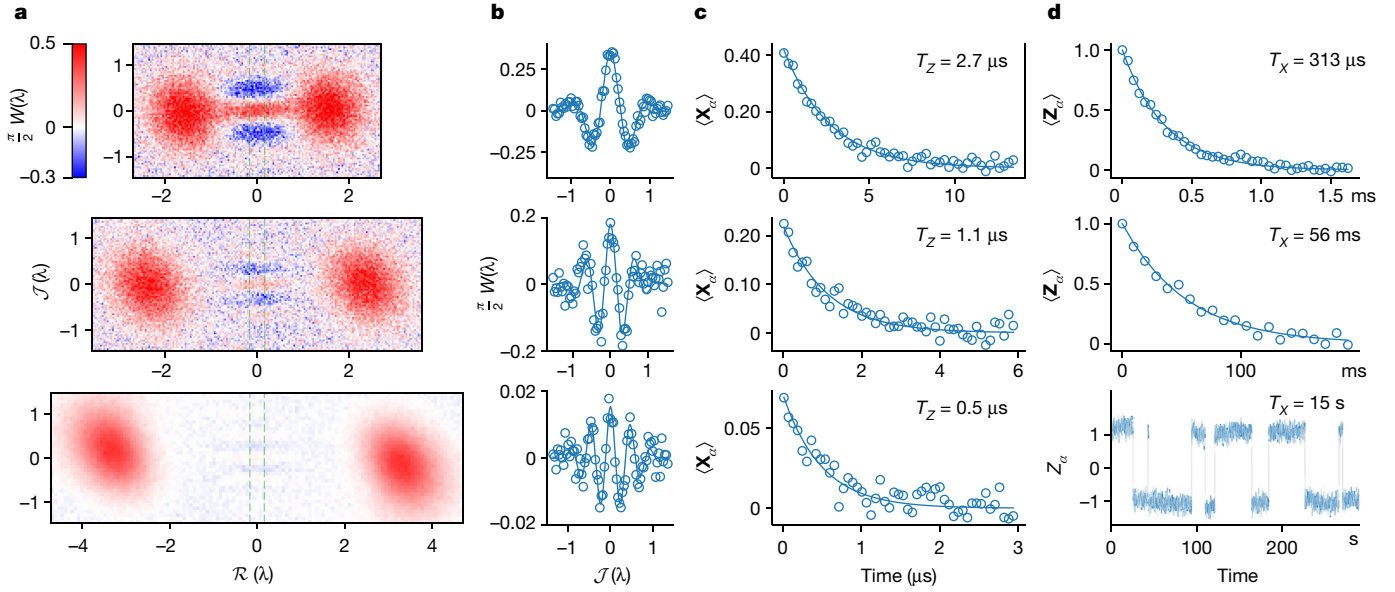
Fig. 3 | Cat-qubit phase-flip and bit-flip time measurements. Each row of figures represents a photon number, $|\alpha|^2$: 2.5 (top), 5.6 (middle) and 11.3 (bottom). **a**, Measured Wigner functions of the memory state $|+\rangle_\alpha$ prepared in 1 µs. Constraining these maps to sum to one sets an absolute scale for our parity measurement. **b**, Integration of the measured Wigner functions (y axis) over the window delimited by the green dashed lines shown in **a** versus the imaginary axis (x axis). We fit the analytical formula of these oscillations[25] (blue lines) to the data (circles). **c**, Evolution of the expectation value of $\mathbf{X}_\alpha$ (y axis) versus time

(x axis) for a memory state $|+\rangle_\alpha$ prepared in 400 ns. The data (circles) follow an exponential decay (blue line) from which we extracted the phase-flip time, T_Z. **d**, Top and middle: expectation value of $\mathbf{Z}_\alpha$ (y axis) versus time (x axis). The data (circles) follow an exponential decay (solid line) from which we extracted the bit-flip time, T_X. Bottom: real-time trajectory cropped from the full dataset of the memory switching between $Z_\alpha = \pm 1$ (y axis) versus time (x axis). It was acquired by applying a drive on the memory and collecting the buffer fluorescence (solid line) (Supplementary Information section 8E).

coherent Zeno-blocked oscillations around the cat-qubit Z axis[23]. We tuned the drive length to perform a $\pi/2$ rotation reaching the parity-less state $|\psi_2\rangle = (|+\rangle_{\alpha_1} + i |-\rangle_{\alpha_1})/\sqrt{2}$ (refs. 20,32,33). Next, we turned off the memory and buffer drives while the two-photon pump remained active, thereby removing pairs of photons from $|\psi_2\rangle$. By parity conservation, $|+\rangle_{\alpha_1}$ is mapped to $|0\rangle$ and $|-\rangle_{\alpha_1}$ to $|1\rangle$ (ref. 20). When this mapping is adiabatic with respect to $\kappa_{\mathrm{conf}}^{-1}$ and fast compared with κ_a^{-1}, quantum superpositions are preserved, yielding $|\psi_3\rangle = (|0\rangle + i |1\rangle)/\sqrt{2}$ (ref. 24). In practice, we used a square buffer drive of amplitude $\alpha_1 \approx 1.6$ in an attempt to maximize the fidelity of the $\pi/2$ gate around Z while minimizing the loss of coherence during these mappings. Next, maintaining the two-photon pump, we activated a buffer drive $\varepsilon_{d,2} = -g_2^*\alpha_2^2$, where α_2 is real. The minus sign on the buffer drive translates into a pure imaginary amplitude for the stabilized coherent states. This maps $|0\rangle \rightarrow |+\rangle_{i\alpha_2}$, $|1\rangle \rightarrow -i |-\rangle_{i\alpha_2}$ (ref. 20), and following the same reasoning, $|\psi_3\rangle \rightarrow |\psi_4\rangle = |i\alpha_2\rangle$ (ref. 24). Conversely, an odd parity, ρ_{odd}, would be mapped to $|-i\alpha_2\rangle$. Information on the parity of $\rho_{\mathrm{even/odd}}$ is now encoded on the amplitude of coherent states $|\pm i\alpha_2\rangle$. Finally, the two-photon pump was turned off and the memory was displaced by $\mathcal{D}_{i\alpha_2}$. The longitudinal pump ε_p^1 is activated to distinguish between 0 and $4|\alpha_2|^2$ photons in the memory by heterodyne detection of the buffer. Note that the value of α_2 can be tuned to optimize the fidelity of the longitudinal read-out. Preceding this entire sequence by a memory displacement of amplitude λ therefore measures $W(\lambda)$. We demonstrated this tomography protocol by measuring the Wigner functions of the vacuum $|0\rangle$, Fock state $|1\rangle$ and $|\pm\rangle_\alpha$ (Fig. 2c). The vacuum was prepared simply by waiting for several κ_a^{-1} for the memory to settle in its thermodynamic equilibrium. Preparing $|+\rangle_\alpha$ required the activation of a two-photon pump and buffer drive for several $\kappa_{\mathrm{conf}}^{-1}$. Preparing $|-\rangle_\alpha$ required an additional memory drive to perform a full Zeno-blocked π rotation. Finally, from this state, switching off the buffer drive while the two-photon pump remained active prepared Fock state $|1\rangle$ by parity conservation.

The measurements of phase-flip and bit-flip times of our cat qubit are displayed in Fig. 3. We prepared $|+\rangle_\alpha$ for various average photon

numbers $|\alpha|^2$ by starting from a memory mode in the vacuum and activating the corresponding buffer-drive amplitude and two-photon pump. The preparation duration (400 ns or 1 µs; Fig. 3) was chosen to be longer than $1/\kappa_{\mathrm{conf}} \approx 120$ ns, ensuring there was sufficient time to reach the steady-state manifold, and on par with $T_Z \approx 490$ ns for the largest states at 11.3 photons, ensuring the preservation of measurable quantum coherence. Using our tomography tool, we imaged the Wigner functions of these states and observed interference fringes that take negative values. Although the contrast of these fringes reduces with increasing $|\alpha|^2$, they remain visible up to $|\alpha|^2 \approx 11.3$ photons (Fig. 3a,b). Note that in the cat-qubit code space, $\langle\mathbf{X}_\alpha\rangle = \langle\mathbf{P}\rangle$, so we could extract the phase-flip time by monitoring the photon-number parity decay over time. We measured phase-flip times ranging from $T_Z = 2.7$ µs for $|\alpha|^2 = 2.5$ to $T_Z = 490$ ns for $|\alpha|^2 = 11.3$ (Fig. 3c). Finally, we monitored the switching between $|\pm\alpha\rangle$ over time (Fig. 3d). To do this, we prepared $|+\alpha\rangle$ by displacing the memory from the vacuum before applying the two-photon pump and a buffer drive, the amplitude of which was adjusted to stabilize $|\pm\alpha\rangle$ for a variable time t. During this time, the state may switch to $|-\alpha\rangle$, causing a bit-flip. We detected the population of $|\alpha\rangle$ at time t by setting the buffer drive to map $|\pm\alpha\rangle \rightarrow |\pm\alpha'\rangle$ where $\alpha' \approx 2.1$, then interrupting the pump and buffer drive, and finally displacing the memory by α'. This maps $|-\alpha'\rangle \rightarrow |0\rangle$ and $|\alpha'\rangle \rightarrow |2\alpha'\rangle$. Next, we activated the longitudinal pump to distinguish between these two states. For bit-flip times exceeding around 100 ms, this method leads to impractically long acquisition times. Instead, for long bit-flip times that occur at $|\alpha|^2 \gtrsim 7$, we sampled the real-time trajectory of the memory field. After initializing the memory in $|\alpha\rangle$ and activating the two-photon exchange, we applied a weak drive of amplitude ε_Z on the memory for 250 µs every millisecond. This slightly displaced the state out of the steady-state manifold. In response to this perturbation, the buffer develops an average field amplitude $\langle\mathbf{b}\rangle = \mp\frac{\varepsilon_Z}{2\alpha^* g_2}$ depending on the state $|\pm\alpha\rangle$ in the memory[34] (Supplementary Information section 8E). This field is then integrated by heterodyne detection (Fig. 3d, bottom) for a pulse duration of $T_{\mathrm{int}} = 250$ µs. For $\alpha^2 \gtrsim 7$, $T_Z \ll T_{\mathrm{int}} \ll T_X$ and hence
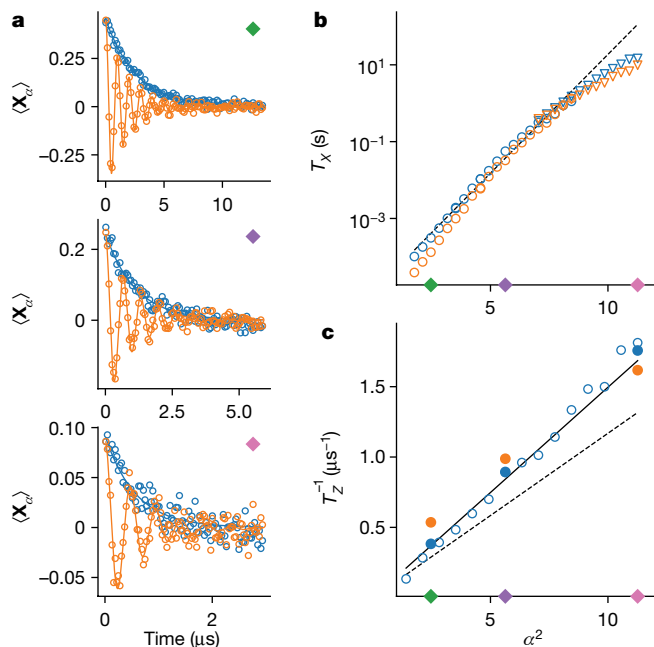
Article

Fig. 4 | Quantum control that preserves bit-flip protection. a, The cat qubit is initialized in $|+\rangle_\alpha$ for $|\alpha|^2 = 2.5$ (top), 5.6 (middle) and 11.3 (bottom) with a preparation duration of 400 ns, and the expectation value of $\mathbf{X}_\alpha$ (y axis) is measured (open circles) over time (x axis). In the presence of a memory drive (orange), the cat qubit undergoes coherent Zeno-blocked oscillations around its Z axis. These oscillations decay exponentially with time. The decay in the absence of oscillations (blue) is superimposed for ease of reference. **b**, The bit-flip time (y axis, log scale) increases exponentially with photon number (x axis), multiplying by 4.2 for each added photon, up to about 7 photons. It is extracted from the measured (open circles) or simulated (dashed line) average population transfer over time between $|\pm\alpha\rangle$, or from measured single real-time trajectories (triangles). **c**, Dephasing rate (y axis) as a function of photon number (x axis). It follows a linear trend (solid line) with a slope that is 25% steeper than the one given by the memory dissipation rate, κ_a (dashed line). The data points (circles) corresponding to the panels in **a** are shown as filled circles. The data in **b** and **c** were recorded in the absence (blue) or presence (orange) of a memory drive of the same amplitude as the one in **a**. In **b** and **c**, the coloured diamonds refer to the indicated panels in **a**.

we could observe bit-flip events in real time, so T_X could be estimated quite accurately from a single trace lasting around $100\,T_X$. Using these methods, we could measure T_X for $|\alpha|^2 = 2.5$, 5.6 and 11.3, and observe a large increase from 313 µs to 56 ms and then 15 s.

We demonstrate quantum control of our cat qubit and its effect on bit-flip protection in Fig. 4. After preparing the cat qubit in $|+\rangle_\alpha$, we added a drive of amplitude ε_Z on the memory mode. The interplay of this coherent drive and two-photon dissipation induces Zeno-blocked oscillations[23] at angular frequency $\Omega_Z = 4|\alpha|\varepsilon_Z$ (ref. 18), as well as a drive-induced dephasing that increases with ε_Z (Supplementary Information section 8F). For $|\alpha|^2 = 11.3$, we observed a π rotation in 235 ns. Because the benefit of the cat qubit is to minimize the hardware overhead for error correction by eliminating the need for active bit-flip correction, it is crucial that we verify that our quantum manipulations do not break bit-flip protection. We measured the scaling of errors for $|\alpha|^2 \in [1.4, 11.3]$, a range on which we can measure both the phase-flip and the bit-flip rates (Fig. 4b,c). We saw the bit-flip time multiply by 4.2 for every added photon, culminating at 15 s. Importantly, in the presence of the continuous memory drive, the bit-flip only slightly reduces, remaining above 10 s for $|\alpha|^2 = 11.3$. However, the measured dephasing rate T_Z^{-1} increases linearly with $|\alpha|^2$, closely following the theoretical prediction $\Gamma_Z^{\kappa_a} = 2\kappa_a|\alpha|^2$. Notably, the oscillator lifetime extracted from a linear fit to the data is 25% larger than the one obtained from spectroscopy,

possibly because of the interplay of the strong two-photon pump and uncontrolled parametric processes.

In conclusion, our experiment demonstrates quantum tomography and coherent control of a cat qubit without breaking bit-flip protection up to bit-flip times of 10 s. This constitutes a 10^4-fold improvement over previous cat-qubit implementations and a 10^6-fold enhancement over the oscillator lifetime. We measured a phase-flip time of 490 ns and performed a π rotation around the Z axis in 235 ns. Although we achieved $g_2/\kappa_a \approx 80 \gg 1$, this ratio needs to be further increased to improve measurement fidelity and reduce state preparation and gate errors to below the error correction threshold[5,35]. Possible directions for progress include circuit engineering to increase g_2 (refs. 36,37), optimized gate design[34,38] and the integration of recent advances in nanofabrication[28,39,40] to improve the oscillator lifetime by at least one order of magnitude. With these improvements in hand, we hope to assemble multiple cat qubits in hardware-efficient error-correcting architectures[5,6,8,13] and operate them to correct phase-flips without breaking bit-flip protection.

Online content

Any methods, additional references, Nature Portfolio reporting summaries, source data, extended data, supplementary information, acknowledgements, peer review information; details of author contributions and competing interests; and statements of data and code availability are available at https://doi.org/10.1038/s41586-024-07294-3.

1. Google Quantum AI Suppressing quantum errors by scaling a surface code logical qubit. *Nature* **614**, 676–681 (2023).
2. Aliferis, P. & Preskill, J. Fault-tolerant quantum computation against biased noise. *Phys. Rev. A* **78**, 052331 (2008).
3. Webster, P., Bartlett, S. D. & Poulin, D. Reducing the overhead for quantum computation when noise is biased. *Phys. Rev. A* **92**, 062309 (2015).
4. Tuckett, D. K., Bartlett, S. D. & Flammia, S. T. Ultrahigh error threshold for surface codes with biased noise. *Phys. Rev. Lett.* **120**, 050505 (2018).
5. Guillaud, J. & Mirrahimi, M. Repetition cat qubits for fault-tolerant quantum computation. *Phys. Rev. X* **9**, 041053 (2019).
6. Darmawan, A. S., Brown, B. J., Grimsmo, A. L., Tuckett, D. K. & Puri, S. Practical quantum error correction with the XZZX code and Kerr-cat qubits. *PRX Quantum* **2**, 030345 (2021).
7. Ruiz, D., Guillaud, J., Leverrier, A., Mirrahimi, M. & Vuillot, C. LDPC-cat codes for low-overhead quantum computing in 2D. Preprint at https://arxiv.org/abs/2401.09541 (2024).
8. Puri, S. et al. Bias-preserving gates with stabilized cat qubits. *Sci. Adv.* **6**, eaay5901 (2020).
9. Guckenheimer, J. & Holmes, P. in *Nonlinear Oscillations, Dynamical Systems, and Bifurcations of Vector Fields* 1–65 (Springer, 1983).
10. Muppalla, P. R. et al. Bistability in a mesoscopic Josephson junction array resonator. *Phys. Rev. B* **97**, 024518 (2018).
11. Mabuchi, H. Nonlinear interferometry approach to photonic sequential logic. *Appl. Phys. Lett.* **99**, 153103 (2011).
12. Nielsen, M. A. & Chuang, I. L. *Quantum Computation and Quantum Information: 10th Anniversary Edition* (Cambridge Univ. Press, 2010).
13. Chamberland, C. et al. Building a fault-tolerant quantum computer using concatenated cat codes. *PRX Quantum* **3**, 010329 (2022).
14. Fowler, A. G., Mariantoni, M., Martinis, J. M. & Cleland, A. N. Surface codes: towards practical large-scale quantum computation. *Phys. Rev. A* **86**, 032324 (2012).
15. Zurek, W. H. Decoherence, einselection, and the quantum origins of the classical. *Rev. Mod. Phys.* **75**, 715–775 (2003).
16. Wolinsky, M. & Carmichael, H. J. Quantum noise in the parametric oscillator: from squeezed states to coherent-state superpositions. *Phys. Rev. Lett.* **60**, 1836–1839 (1988).
17. Leghtas, Z. et al. Confining the state of light to a quantum manifold by engineered two-photon loss. *Science* **347**, 853–857 (2015).
18. Mirrahimi, M. et al. Dynamically protected cat-qubits: a new paradigm for universal quantum computation. *New J. Phys.* **16**, 045014 (2014).
19. Lescanne, R. et al. Exponential suppression of bit-flips in a qubit encoded in an oscillator. *Nat. Phys.* **16**, 509–513 (2020).
20. Grimm, A. et al. Stabilization and operation of a Kerr-cat qubit. *Nature* **584**, 205–209 (2020).
21. Frattini, N. E. et al. The squeezed Kerr oscillator: spectral kissing and phase-flip robustness. Preprint at https://arxiv.org/abs/2209.03934 (2022).
22. Berdou, C. et al. One hundred second bit-flip time in a two-photon dissipative oscillator. *PRX Quantum* **4**, 020350 (2023).
23. Touzard, S. et al. Coherent oscillations inside a quantum manifold stabilized by dissipation. *Phys. Rev. X* **8**, 021005 (2018).
24. Albert, V. V. et al. Holonomic quantum control with continuous variable systems. *Phys. Rev. Lett.* **116**, 140502 (2016).

25. Haroche, S. & Raimond, J.-M. *Exploring the Quantum: Atoms, Cavities, and Photons* (Oxford Univ. Press, 2006).

26. Gottesman, D., Kitaev, A. & Preskill, J. Encoding a qubit in an oscillator. *Phys. Rev. A* **64**, 012310 (2001).

27. Girvin, S. M. in *Quantum Machines: Measurement and Control of Engineered Quantum Systems* (eds Devoret, M. et al.) 113–256 (Oxford Univ. Press, 2014).

28. Place, A. P. M. et al. New material platform for superconducting transmon qubits with coherence times exceeding 0.3 milliseconds. *Nat. Commun.* **12**, 1779 (2021).

29. Flurin, E. *The Josephson mixer: a Swiss army knife for microwave quantum optics*. Phd thesis, ENS Paris (2014).

30. Aspelmeyer, M., Kippenberg, T. J. & Marquardt, F. Cavity optomechanics. *Rev. Mod. Phys.* **86**, 1391–1452 (2014).

31. Touzard, S. et al. Gated conditional displacement readout of superconducting qubits. *Phys. Rev. Lett.* **122**, 080502 (2019).

32. Yurke, B. & Stoler, D. The dynamic generation of Schrödinger cats and their detection. *Physica B+C* **151**, 298–301 (1988).

33. Kirchmair, G. et al. Observation of quantum state collapse and revival due to the single-photon Kerr effect. *Nature* **495**, 205–209 (2013).

34. Gautier, R,., Mirrahimi, M. & Sarlette, A. Designing high-fidelity Zeno gates for dissipative cat qubits. *PRX Quantum* **4**, 040316 (2023).

35. Gautier, R., Sarlette, A. & Mirrahimi, M. Combined dissipative and Hamiltonian confinement of cat qubits. *PRX Quantum* **3**, 020339 (2022).

36. Aiello, G. et al. Quantum bath engineering of a high impedance microwave mode through quasiparticle tunneling. *Nat. Commun.* **13**, 7146 (2022).

37. Marquet, A. et al. Autoparametric resonance extending the bit-flip time of a cat qubit up to 0.3 s. Preprint at https://arxiv.org/abs/2307.06761 (2024).

38. Eickbusch, A. et al. Fast universal control of an oscillator with weak dispersive coupling to a qubit. *Nat. Phys.* **18**, 1464–1469 (2022).

39. Wang, C. et al. Towards practical quantum computers: transmon qubit with a lifetime approaching 0.5 milliseconds. *npj Quantum Inf.* **8**, 3 (2022).

40. Kono, S. et al. Mechanically induced correlated errors on superconducting qubits with relaxation times exceeding 0.4 milliseconds. Preprint at https://arxiv.org/abs/2305.02591 (2023).

Article

Author contributions P.C.-I., R.L., S.J. and Z.L. conceived the experiment. U.R. and A.B. designed the chip with support from M.H. and F.R. U.R. and A.B. measured the device and analysed the data. E.A. and N.P. fabricated the chip. R.G., J.C., A.M., L.-A.S., P.R., A.S. and M.M. provided theory support. U.R., A.B. and Z.L. wrote the paper with input from all authors.